



Topology optimization of dispersive plasmonic nanostructures in the time-domain

EMADELDEEN HASSAN^{1,2,3,4}  AND ANTONIO CALÀ LESINA^{1,5} 

¹Hannover Centre for Optical Technologies, Institute for Transport and Automation Technology (Faculty of Mechanical Engineering), and Cluster of Excellence PhoenixD, Leibniz University Hannover, 30167 Hannover, Germany

²Department of Electronics and Electrical Communications, Menoufia University, Menouf 32952, Egypt

³Department of Applied Physics and Electronics, Umeå University, SE-901 87 Umeå, Sweden

⁴emadeldeen.hassan@umu.se

⁵antonio.calalesina@hot.uni-hannover.de

Abstract: Topology optimization techniques have been applied in integrated optics and nanophotonics for the inverse design of devices with shapes that cannot be conceived by human intuition. At optical frequencies, these techniques have only been utilized to optimize nondispersive materials using frequency-domain methods. However, a time-domain formulation is more efficient to optimize materials with dispersion. We introduce such a formulation for the Drude model, which is widely used to simulate the dispersive properties of metals, conductive oxides, and conductive polymers. Our topology optimization algorithm is based on the finite-difference time-domain (FDTD) method, and we introduce a time-domain sensitivity analysis that enables the evaluation of the gradient information by using one additional FDTD simulation. The existence of dielectric and metallic structures in the design space produces plasmonic field enhancement that causes convergence issues. We employ an artificial damping approach during the optimization iterations that, by reducing the plasmonic effects, solves the convergence problem. We present several design examples of 2D and 3D plasmonic nanoantennas with optimized field localization and enhancement in frequency bands of choice. Our method has the potential to speed up the design of wideband optical nanostructures made of dispersive materials for applications in nanoplasmonics, integrated optics, ultrafast photonics, and nonlinear optics.

Published by Optica Publishing Group under the terms of the [Creative Commons Attribution 4.0 License](https://creativecommons.org/licenses/by/4.0/). Further distribution of this work must maintain attribution to the author(s) and the published article's title, journal citation, and DOI.

1. Introduction

The last decade has witnessed an exponential increase of research in nanophotonics. Plasmonic and dielectric nanostructured materials, such as metasurfaces and metamaterials, have been developed to engineer the properties of light beyond what is allowed by bulk optical devices [1,2], thus leading to revolutionary solutions for beam structuring [3], colouring [4], biosensing [5], nanomedicine [6], tunable beam steering [7], and nonlinear generation [8,9], to name a few. Advances in nanofabrication technologies have enabled such technologies by allowing unprecedented design complexity at the nanoscale [5,10]. The opportunities offered by theoretical research and nanofabrication facilities raise the need for new methods to efficiently design and optimize such nanophotonic systems [11,12].

Advances in computing capabilities and numerical methods, such as the finite-difference time-domain (FDTD) [13] and finite-element methods (FEM) [14], empowered the design of nanophotonic devices while shortening their design cycle. Conventionally, a design cycle starts from a given layout. The layout is then parameterized and various techniques are employed to explore the parameters' space. This offers opportunities to find new designs with improved performance or that satisfy multi-objectives. However, exploring large parameter spaces raises

computational challenges. Techniques such as parameters sweep or stochastic optimization methods, e.g., genetic algorithms, are computationally intractable for large design spaces and only suitable to handle problems with few design parameters [15]. Deep learning algorithms are also an option, but require large data sets for training, and still not well established [16–18].

Topology optimization (TopOpt) is a robust inverse design approach [19,20]. It was initially introduced to optimize mechanical structures [21], then it has been successfully extended to various engineering disciplines, including acoustics [22], fluids [23], and electromagnetics [24–28]. Typically, TopOpt problems are solved using gradient-based optimization methods, where the gradient of the objective function is computed using efficient methods such as the adjoint-field method [29,30]. Optimization problems that include millions or even billions of design variables have enabled novel conceptual designs [31]. In electromagnetics, TopOpt was used to optimize non-dispersive dielectric devices in the microwave and optical regimes [32–35]. In addition, it was used to design plasmonic antennas using frequency-domain methods [36–38]. Christiansen et al. [37] proposed a non-linear interpolation scheme that was successful to enable TopOpt of plasmonic antennas near their surface plasma frequency using the FEM method.

Structural perturbations or changes in material properties, caused for example by fabrication tolerance or temperature variations, raise the demand to account for the broadband performance of optical components [39]. At optical and near-infrared wavelengths, various materials exhibit dispersion, that can be modelled via Drude, Lorentz, or critical-points functions [13,40,41]. Below their plasma frequency, the Drude model is commonly used to describe the dispersive properties of metals such as silver, gold, and aluminum [42]. The model also describes the permittivity of conductive oxides, such as indium tin oxide (ITO) [43], and conductive polymers [44], including their dielectric and epsilon-near-zero regions.

In this paper, we introduce TopOpt of dispersive optical materials in the time-domain and aim at broadband designs. We base our algorithm on the FDTD method [13] and the Drude model to describe the material dispersion. To the best of our knowledge, this is the first time the FDTD method is used for TopOpt of plasmonic devices in the time domain. To present the algorithm, we conduct the optimization of plasmonic nanoantennas, with the goal to maximize the electric energy in a specified region by finding the distribution of the electric permittivity in a design domain. To evaluate the gradient of the objective function efficiently, we employ the adjoint-field method and provide sensitivity analysis based on Maxwell's equations in their first-order form. During the optimization, the interpolation of the design material between dielectric and metal enables the surface plasmon frequency ω_{sp} to fall within the frequency band of interest [45,46]. Plasmonic effects, such as field localization and enhancement, are amplified close to ω_{sp} . This leads to hot-spots within the optimization domain that prevent the algorithm from converging to well performing designs. To overcome these convergence issues, we exploit the conductivity term in Maxwell's equations to introduce an artificial damping. This damping counteracts the high-field localization during the optimization process and enables the algorithm to converge to good designs. The developed algorithm is demonstrated by optimizing 2D and 3D silver nanoantennas operating near plasma and infrared frequencies. In all cases, the algorithm produces novel designs with outstanding performance, thus demonstrating its use for the automatic design of dispersive optical nanostructures and metamaterials.

2. Optimization problem setup

In this section, we present the setup of the optimization problem that will be used to inverse design 2D and 3D nanostructures. The computational domain Ω consists of $\Omega_g \cup \Omega_d \cup \Omega_s \cup \Omega_{PML}$, as shown in Fig. 1(a). The domain Ω_g is an observation region where the electric energy is to be maximized. We assume that Ω_g is a dispersionless dielectric medium with relative permittivity ϵ_g and has an area $w_g \times h_g$. Inside the design domain $\Omega_d = w_d \times h_d$, we aim to distribute a dispersive material to form the nanoantenna structure. We consider materials with relative permittivity

described by the Drude model:

$$\varepsilon^{Drude}(\omega) = \varepsilon_\infty - \frac{\psi}{\omega^2 - j\omega\gamma_p}, \quad (1)$$

where ε_∞ is the high-frequency permittivity; γ_p is the collision rate; $\psi = \omega_p^2 = \frac{ne^2}{m_e\varepsilon_0}$ is the square of the plasma frequency; ε_0 is the vacuum permittivity; n , m_e , and e are the electrons' density, effective mass, and charge, respectively. We use the $e^{j\omega t}$ convention.

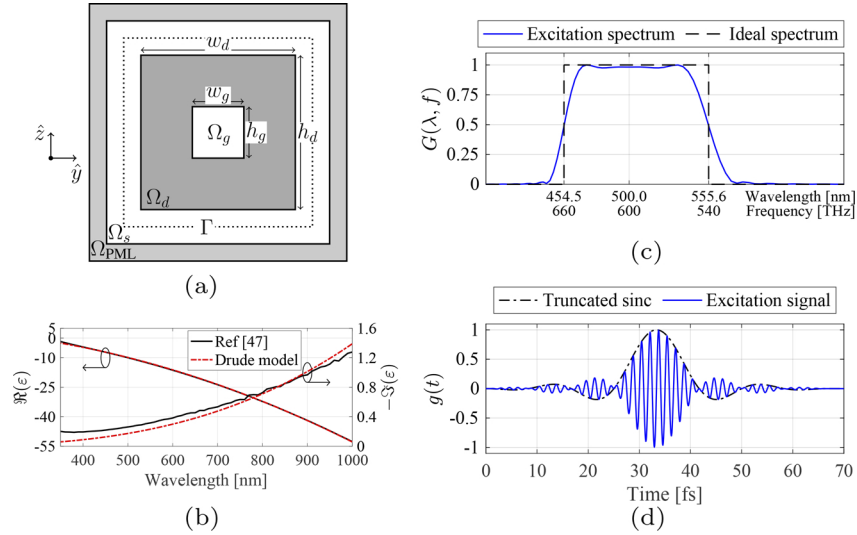


Fig. 1. (a) Ω_g is the observation domain, Ω_d is the design domain, Ω_s is the background medium, and Ω_{PML} is a perfect matched layer. The boundary Γ is used for plane-wave injection. (b) Complex permittivity of silver [47], and fitting via the Drude model. (c) Frequency and (d) time domain plots of a truncated sinc signal with a bandwidth of 20% at half-maximum and modulating a carrier signal with a frequency of 600 THz.

In this paper, we consider silver in the wavelength range 350–1000 nm, where we fit its measured complex permittivity [47], via a Drude model with parameters $\varepsilon_\infty = 4.469$, $\omega_p = 1.426 \times 10^{16}$ rad/s, and $\gamma_p = 4.571 \times 10^{13}$ rad/s, as shown in Fig. 1(b). The background space Ω_s hosts the design domain Ω_d , and has a constant relative permittivity ε_s . For simplicity, we use $\varepsilon_s = \varepsilon_g = 1$, but deviation from these values is also possible. The computational domain is terminated by perfectly matched layers Ω_{PML} . In our analysis, we use the total-field scattered-field formulation [13] to inject a plane-wave through the boundary Γ , which is located in Ω_s . A similar setup was previously used to optimize TM nanoantennas with frequency-domain methods [36,37].

To optimize in the time-domain, the spectral content of the excitation signal determines the desired bandwidth of the structure under optimization. Ideally, we want to excite the system with a signal that has a rectangular spectrum (see Fig. 1(c)). Unfortunately, this corresponds to a sinc signal of infinite duration. Thus, to keep the simulation time reasonable, the sinc signal is truncated to a few lobes, as shown in Fig. 1(d). Such signal modulates a carrier with a frequency corresponding to the center of the spectral window of interest. In addition, we use a Hanning window to reduce the ripples in the excitation spectrum.

We formulate the conceptual optimization problem

$$\begin{aligned} & \underset{\varepsilon(x) \in [\varepsilon_s, \varepsilon^{Drude}(\omega)]}{\text{maximize}} && W \\ & \text{subject to: the governing equations,} && \\ & && \text{and a specified spectral content,} \end{aligned} \quad (2)$$

where

$$W = \frac{1}{2} \int_{\Omega_g} \int_0^T \varepsilon_g \mathcal{E}^2 dt d\Omega \quad (3)$$

is the electric energy in Ω_g , \mathcal{E} is the time-dependent electric field, and T is the observation time. The domain Ω_g corresponds to the gap of a plasmonic nanoantenna or to a focus region where the energy is collimated by the designed structure. A detailed description of the numerical treatments of the optimization problem is given in Section 3.

2.1. Density-based interpolation and convergence issues

In density-based TopOpt, we use the permittivity function of the material as our design variable. For each point x in Ω_d we want the permittivity at that point to be either that of the Drude material $\varepsilon^{Drude}(\omega)$ or that of the background space ε_s . In order to interpolate between the background space and the design material, a density variable ρ_i is introduced to describe the material at each edges of the computational grid in Ω_d . The vector $\boldsymbol{\rho} = [\rho_1 \rho_2 \dots \rho_i \dots \rho_M]$ is used to hold the M design variables of the optimization problem. Since we aim to use gradient-based methods to solve the TopOpt problem, the entries of the design vector are allowed to attain values between 0 and 1 during the optimization process. However, to obtain a manufacturable design, the final density vector must hold only the binary values 0 or 1. We map each design variable ρ_i to the physical material parameters using:

$$\varepsilon(\omega, \rho_i) = \varepsilon_{\infty i} - \frac{\psi_i}{\omega^2 - j\omega\gamma_p} - j \frac{\sigma_i}{\omega\varepsilon_0}, \quad (4)$$

where

$$\varepsilon_{\infty i} = \varepsilon_s + \rho_i(\varepsilon_{\infty} - \varepsilon_s), \quad (5a)$$

$$\psi_i = \psi_s + \rho_i(\psi - \psi_s), \quad (5b)$$

$$\sigma_i = \rho_i(1 - \rho_i)\sigma_{\max} \quad (5c)$$

are our three design variables (the dependence on ρ_i is carried by the i subscript). The parameters ψ_i and $\varepsilon_{\infty i}$ perform a linear interpolation between the physical parameters of the background space $\{\varepsilon_s, \psi_s\}$ and those of the design material $\{\varepsilon_{\infty}, \psi\}$. We use $\psi_s = \psi/100$ to ensure $\psi > 0$, thus avoiding the singularity in Eq. (21). In fact, the value $\rho_i = 1$ corresponds to the Drude model $\varepsilon^{Drude}(\omega)$, and $\rho_i = 0$ sufficiently approximates the background permittivity ε_s . To overcome convergence issues, we modify the Drude model to include an artificial conductivity σ_i , that plays a temporary role only during the optimization. To do so, we use a parabolic profile, so that the conductivity is zero for $\rho_i = 0$ and $\rho_i = 1$, and reaches its maximum value σ_{\max} for $\rho_i = 0.5$. The value σ_{\max} must be carefully chosen, as discussed later. Fig. 2(a)-(c) show the interpolation between the permittivity of free space ($\rho = 0$) and silver ($\rho = 1$) using the design permittivity model $\varepsilon(\omega, \rho)$ in Eq. 4, where we drop the index i for brevity.

The presence of metal and dielectric in the design domain leads to localization and enhancement of the electric field due to surface plasmon modes arising during the optimization process. This hinders the convergence of the objective function. To understand the reason for such convergence problem, we use, as an illustrative model, the dispersion relation of surface plasmon polaritons (SSPs) at a flat interface between a dielectric ε_s and our design material $\varepsilon(\omega, \rho)$ [45,46]:

$$\beta_{||}(\omega, \rho) = k_0 \sqrt{\frac{\varepsilon(\omega, \rho)\varepsilon_s}{\varepsilon(\omega, \rho) + \varepsilon_s}} \quad (6a)$$

$$k_{\perp s}(\omega, \rho) = \sqrt{\beta_{||}^2 - k_0^2 \varepsilon_s} \quad (6b)$$

$$k_{\perp m}(\omega, \rho) = \sqrt{\beta_{||}^2 - k_0^2 \varepsilon(\omega)} \quad (6c)$$

where $\beta_{||}$ is the propagation constant parallel to the interface; $k_{\perp s}$ and $k_{\perp m}$ are attenuation factors normal to the interface inside the dielectric and metal, respectively; and $k_0 = \omega\sqrt{\mu_0\varepsilon_0}$, as shown

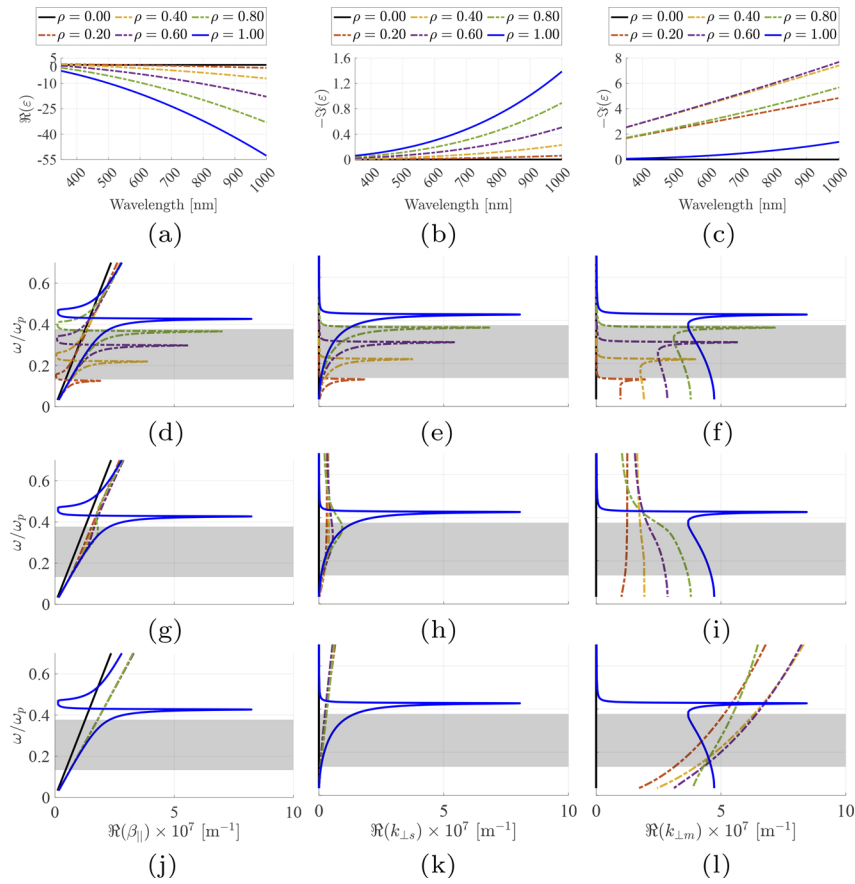


Fig. 2. Interpolating between free-space permittivity ($\rho=0$) and silver ($\rho=1$). (a) Real and (b) Imaginary part of $\epsilon(\omega, \rho)$ when $\sigma_{\max}=0$ S/m. (c) Imaginary part of $\epsilon(\omega, \rho)$ when $\sigma_{\max}=5 \times 10^5$ S/m (the real part is the same as (a)). Dispersion diagrams of the surface plasmon polaritons when interpolating between air and silver using (d)-(f) $\sigma_{\max}=0$ S/m, (g)-(i) $\sigma_{\max}=5 \times 10^5$ S/m, and (j)-(l) $\sigma_{\max}=5 \times 10^6$ S/m.

in Figs. 2(d)-(f) for values of ρ between air ($\rho=0$) and silver ($\rho=1$). The horizontal gray strip marks the wavelength interval of interest 350–1000 nm. Inspecting the silver case ($\rho=1$), we see that the value of $\beta_{||}$ reaches a maximum close to the surface plasmon frequency ω_{sp} [45,46], which by design is located outside the wavelength window of interest. The values of $k_{\perp s}$ and $k_{\perp m}$ also reach a maximum close to ω_{sp} , which indicates a large wave attenuation in the directions normal to the interface. In other words, the wave propagates with the wavenumber $\beta_{||}$, and it is spatially highly localized at the interface region. The range of frequencies $\omega > \omega_{sp}$ is not of interest for SPPs. For intermediate values of ρ , the material permittivity changes from metal to dielectric, and ω_{sp} moves across the wavelength window of interest. This results in moving the peaks of the dispersion curves into the wavelength window of interest, as shown in Figs. 2(d)-(f) for $\sigma_{\max}=0$ S/m. The high-field localization, associated with large amplitudes of $k_{\perp s}$, $k_{\perp m}$ and $\beta_{||}$, counteracts the objective function that aims to maximize the electric field in the domain Ω_g . This conflict prevents the algorithm from converging to well-performing designs.

With the aim to reduce the peaks in the dispersion diagrams at intermediate values of ρ , we estimate the value of σ_{\max} based on a parameter sweep. Plots for our chosen σ_{\max} value (i.e., $\sigma_{\max}=5 \times 10^5$ S/m) are shown in Figs. 2(g)-(i). A too-large value of σ_{\max} (e.g., $\sigma_{\max}=5 \times 10^6$

S/m) leads to an intermediate material with conductivity higher than silver, as shown in Fig. 2(j)-(l). To conclude, a too-small value of σ_{\max} is not enough to introduce sufficient damping to counteract the plasmonic effects, while a too-large value prevents the algorithm from converging to black and white designs since the structure becomes less lossy.

3. Methods

3.1. Governing equations and sensitivity analysis

Inside the analysis domain, that we assume source-free and non-magnetic with permeability μ_0 , the time-dependent electric field \mathcal{E} and magnetic field \mathcal{H} are governed by Maxwell's equations

$$\partial_t \mathcal{D} - \nabla \times \mathcal{H} = \mathbf{0}, \quad (7a)$$

$$\mu_0 \partial_t \mathcal{H} + \nabla \times \mathcal{E} = \mathbf{0}, \quad (7b)$$

where the electric displacement field \mathcal{D} models the optical response of the materials through the frequency domain relation

$$\mathcal{D}(\omega) = \varepsilon_0 \varepsilon(\omega) \mathcal{E}(\omega). \quad (8)$$

In our case, we use the design permittivity model

$$\varepsilon(\omega) = \varepsilon_\infty - \frac{\psi}{\omega^2 - j\omega\gamma_p} - j \frac{\sigma}{\omega\varepsilon_0}, \quad (9)$$

that consists of a Drude model and an additional artificial conductivity term that operates only during the optimization process to guarantee convergence. By substituting Eq. (9) and Eq. (8) into Eq. (7a), we rewrite Eqs. (7) as

$$\varepsilon_0 \varepsilon_\infty \partial_t \mathcal{E} + \mathcal{J} + \sigma \mathcal{E} - \nabla \times \mathcal{H} = \mathbf{0}, \quad (10a)$$

$$\partial_t \mathcal{J} + \gamma_p \mathcal{J} - \varepsilon_0 \psi \mathcal{E} = \mathbf{0}, \quad (10b)$$

$$\mu_0 \partial_t \mathcal{H} + \nabla \times \mathcal{E} = \mathbf{0}, \quad (10c)$$

where the dispersion of the medium is embedded in the polarization current density \mathcal{J} , with Eq. (10b) being the time-domain equivalent of

$$\mathcal{J}(\omega) = \frac{\varepsilon_0 \psi}{j\omega + \gamma_p} \mathcal{E}(\omega). \quad (11)$$

We solve the design problem by using a gradient-based optimization method. To do so, we need derivatives of the objective function with respect to the design variables ε_∞ , ψ , and σ . We use the adjoint-field method to derive expressions for such derivatives. Assuming that the design variables are perturbed by $\delta\varepsilon_\infty$, $\delta\psi$, and $\delta\sigma$, the corresponding first variations of W are

$$\delta_{\varepsilon_\infty} W = \int_{\Omega_g} \int_0^T \varepsilon_g \mathcal{E} \delta_{\varepsilon_\infty} \mathcal{E} dt d\Omega, \quad (12a)$$

$$\delta_\psi W = \int_{\Omega_g} \int_0^T \varepsilon_g \mathcal{E} \delta_\psi \mathcal{E} dt d\Omega, \quad (12b)$$

$$\delta_\sigma W = \int_{\Omega_g} \int_0^T \varepsilon_g \mathcal{E} \delta_\sigma \mathcal{E} dt d\Omega. \quad (12c)$$

To find explicit expressions for Eqs. (12), we use the system governing Eqs. (10) and employ the adjoint-field method [29,30]. In the following, we derive an explicit relation for $\delta_\psi W$. To simplify the derivation, we drop the domain Ω_{PML} and consider Γ as the external boundary of

the analysis domain Ω , see Fig. 1(a). In addition, we drop the differential dt and $d\Omega$ since they can be inferred from the limits of the integrals. We consider the initial-boundary-value-problem,

$$\varepsilon_0 \varepsilon_\infty \partial_t \mathcal{E} + \mathcal{J} + \sigma \mathcal{E} - \nabla \times \mathcal{H} = \mathbf{0} \quad \text{in } \Omega, t > 0 \tag{13a}$$

$$\partial_t \mathcal{J} + \gamma_p \mathcal{J} - \varepsilon_0 \psi \mathcal{E} = \mathbf{0} \quad \text{in } \Omega, t > 0 \tag{13b}$$

$$\mu_0 \partial_t \mathcal{H} + \nabla \times \mathcal{E} = \mathbf{0} \quad \text{in } \Omega, t > 0 \tag{13c}$$

$$\mathcal{E}_t + \eta \mathbf{n} \times \mathcal{H} = g \quad \text{on } \Gamma, t > 0 \tag{13d}$$

$$\mathcal{E} = \mathbf{0}, \mathcal{J} = \mathbf{0}, \mathcal{H} = \mathbf{0} \quad \text{in } \Omega, t = 0, \tag{13e}$$

where $\eta = \sqrt{\mu_0 / (\varepsilon_0 \varepsilon_s)}$ is the intrinsic impedance of the domain Ω_s , and $\mathcal{E}_t = \mathcal{E} - \mathbf{n}(\mathcal{E} \cdot \mathbf{n})$ with \mathbf{n} denoting the outward unit normal at Γ . The boundary condition (13d) is used to impose an incoming excitation g through Γ . To simplify the notation, the symbol δ is temporarily used to denote the perturbation of the fields with respect to ψ . We differentiate the system of Eqs. (13) with respect to ψ ,

$$\varepsilon_0 \varepsilon_\infty \partial_t \delta \mathcal{E} + \delta \mathcal{J} + \sigma \delta \mathcal{E} - \nabla \times \delta \mathcal{H} = \mathbf{0} \quad \text{in } \Omega, t > 0 \tag{14a}$$

$$\partial_t \delta \mathcal{J} + \gamma_p \delta \mathcal{J} - \varepsilon_0 \psi \delta \mathcal{E} - \varepsilon_0 \mathcal{E} \delta \psi = \mathbf{0} \quad \text{in } \Omega, t > 0 \tag{14b}$$

$$\mu_0 \partial_t \delta \mathcal{H} + \nabla \times \delta \mathcal{E} = \mathbf{0} \quad \text{in } \Omega, t > 0 \tag{14c}$$

$$\delta \mathcal{E}_t + \eta \mathbf{n} \times \delta \mathcal{H} = \mathbf{0} \quad \text{on } \Gamma, t > 0 \tag{14d}$$

$$\delta \mathcal{E} = \mathbf{0}, \delta \mathcal{J} = \mathbf{0}, \delta \mathcal{H} = \mathbf{0} \quad \text{in } \Omega, t = 0. \tag{14e}$$

We define the adjoint fields \mathcal{E}^* , \mathcal{J}^* , and \mathcal{H}^* . We perform the scalar product of Eqs. (14a), (14b), and (14c) with \mathcal{E}^* , $\frac{\mathcal{J}^*}{\varepsilon_0 \psi}$, and \mathcal{H}^* , respectively. We add the result of multiplication, integrating over the whole analysis domain Ω and the observation interval $(0, T)$, and applying integration by parts, we obtain

$$\begin{aligned} & \varepsilon_0 \varepsilon_\infty \mathcal{E}^* \delta \mathcal{E} \Big|_0^T - \int_\Omega \int_0^T \varepsilon_0 \varepsilon_\infty \partial_t \mathcal{E}^* \delta \mathcal{E} + \int_\Omega \int_0^T \mathcal{E}^* \delta \mathcal{J} + \int_\Omega \int_0^T \sigma \mathcal{E}^* \delta \mathcal{E} - \int_\Gamma \int_0^T (\mathbf{n} \times \delta \mathcal{H}) \mathcal{E}^* + \\ & - \int_\Omega \int_0^T (\nabla \times \mathcal{E}^*) \delta \mathcal{H} - \frac{\mathcal{J}^*}{\varepsilon_0 \psi} \delta \mathcal{J} \Big|_0^T + \int_\Omega \int_0^T \partial_t \mathcal{J}^* \frac{\delta \mathcal{J}}{\varepsilon_0 \psi} - \int_\Omega \int_0^T \gamma_p \mathcal{J}^* \frac{\delta \mathcal{J}}{\varepsilon_0 \psi} + \int_\Omega \int_0^T \mathcal{J}^* \delta \mathcal{E} + \\ & + \frac{\mathcal{E} \mathcal{J}^*}{\psi} \delta \psi + \mu_0 \mathcal{H}^* \delta \mathcal{H} \Big|_0^T - \int_\Omega \int_0^T \mu_0 \partial_t \mathcal{H}^* \delta \mathcal{H} + \int_\Gamma \int_0^T (\mathbf{n} \times \delta \mathcal{E}) \mathcal{H}^* + \int_\Omega \int_0^T \nabla \times \mathcal{H}^* \delta \mathcal{E} = \mathbf{0}. \end{aligned} \tag{15}$$

We assume that the adjoint fields satisfy the terminal conditions $\mathcal{E}^* = \mathcal{J}^* = \mathcal{H}^* = \mathbf{0}$ at $t = T$. By arranging the terms in Eq. (15), utilizing Eq. (14d), and adding and subtracting $\delta_\psi W$, we obtain

$$\begin{aligned} & \int_\Omega \int_0^T (-\varepsilon_0 \varepsilon_\infty \partial_t \mathcal{E}^* + \mathcal{J}^* + \sigma \mathcal{E}^* + \nabla \times \mathcal{H}^*) \delta \mathcal{E} + \int_\Omega \int_0^T (\partial_t \mathcal{J}^* - \gamma_p \mathcal{J}^* + \varepsilon_0 \psi \mathcal{E}^*) \frac{\delta \mathcal{J}}{\varepsilon_0 \psi} + \\ & + \int_\Omega \int_0^T (-\partial_t \mu \mathcal{H}^* - \nabla \times \mathcal{E}^*) \delta \mathcal{H} + \int_\Gamma \int_0^T (\mathcal{E}_t^* - \eta \mathbf{n} \times \mathcal{H}^*) \delta \mathcal{H} + \int_\Omega \int_0^T \frac{\mathcal{E} \mathcal{J}^*}{\psi} \delta \psi + \\ & + \delta_\psi W - \int_{\Omega_g} \int_0^T \varepsilon_g \mathcal{E} \delta \mathcal{E} = \mathbf{0}. \end{aligned} \tag{16}$$

Now, if we require

$$-\varepsilon_0 \varepsilon_\infty \partial_t \mathcal{E}^* + \mathcal{J}^* + \sigma \mathcal{E}^* + \nabla \times \mathcal{H}^* = \varepsilon_g \mathcal{E} \quad \text{in } \Omega, t > 0 \tag{17a}$$

$$\partial_t \mathcal{J}^* - \gamma_p \mathcal{J}^* + \varepsilon_0 \psi \mathcal{E}^* = \mathbf{0} \quad \text{in } \Omega, t > 0 \tag{17b}$$

$$\partial_t \mu \mathcal{H}^* + \nabla \times \mathcal{E}^* = \mathbf{0} \quad \text{in } \Omega, t > 0 \tag{17c}$$

$$\mathcal{E}_t^* - \eta \mathbf{n} \times \mathcal{H}^* = \mathbf{0} \quad \text{on } \Gamma, t > 0 \tag{17d}$$

$$\mathcal{E}^* = \mathbf{0}, \mathcal{J}^* = \mathbf{0}, \mathcal{H}^* = \mathbf{0} \quad \text{in } \Omega, t = T, \tag{17e}$$

then Eq. (16) reduces to

$$\delta_\psi W = - \int_\Omega \int_0^T \frac{\mathcal{E} \mathcal{J}^*}{\psi} \delta\psi. \quad (18)$$

Expression (18) is the directional derivative of W when ψ is perturbed by $\delta\psi$. The gradient of W with respect to ψ can be identified as the integral kernel

$$\nabla_\psi W = - \int_0^T \frac{\mathcal{E} \mathcal{J}^*}{\psi}. \quad (19)$$

The adjoint system (17) is a terminal-value-problem which, by changing the time variable (i.e., $t = T - \tau$) and the sign of the magnetic field \mathcal{H}^* (i.e., to preserve the direction of the Poynting vector), can be written as

$$\varepsilon_0 \varepsilon_\infty \partial_\tau \mathcal{E}^* + \mathcal{J}^* + \sigma \mathcal{E}^* - \nabla \times \mathcal{H}^* = \varepsilon_g \overleftarrow{\mathcal{E}} \quad \text{in } \Omega, \tau < T \quad (20a)$$

$$\partial_\tau \mathcal{J}^* + \gamma_p \mathcal{J}^* - \varepsilon_0 \psi \mathcal{E}^* = \mathbf{0} \quad \text{in } \Omega, \tau < T \quad (20b)$$

$$\partial_\tau \mu \mathcal{H}^* + \nabla \times \mathcal{E}^* = \mathbf{0} \quad \text{in } \Omega, \tau < T \quad (20c)$$

$$\mathcal{E}_t^* + \eta \mathbf{n} \times \mathcal{H}^* = \mathbf{0} \quad \text{on } \Gamma, \tau < T \quad (20d)$$

$$\mathcal{E}^* = \mathbf{0}, \mathcal{J}^* = \mathbf{0}, \mathcal{H}^* = \mathbf{0} \quad \text{in } \Omega, \tau = 0, \quad (20e)$$

and (19) becomes

$$\nabla_\psi W = - \int_0^T \frac{\overleftarrow{\mathcal{E}} \mathcal{J}^*}{\psi}, \quad (21)$$

where $\overleftarrow{\mathcal{E}} = \mathcal{E}(T - \tau)$ is the electric field of the forward system (13) reversed in time. The singularity of Eq. (21) can be avoided by ensuring the condition $\psi = \omega_p^2 > 0$. The only difference between the adjoint system (20) and the forward system (13) is the source. In the forward system (13), the source is a plane-wave imposed through the boundary Γ , see Eq. (13d). In the adjoint system (20), the source is the time-reversal of the forward electric field monitored at Ω_g .

By differentiating system (13) with respect to ε_∞ and σ , and following similar procedures as before, we obtain the same adjoint system (20) and the following gradient expressions

$$\nabla_{\varepsilon_\infty} W = - \int_0^T \varepsilon_0 \overleftarrow{\mathcal{E}} \partial_\tau \mathcal{E}^*, \quad (22)$$

$$\nabla_\sigma W = - \int_0^T \overleftarrow{\mathcal{E}} \mathcal{E}^*. \quad (23)$$

Thus, to evaluate the gradient of the objective function, we solve the forward system (13) and the adjoint system (20), then we use Eqs. (21), (22), and (23) to form the full gradient components.

3.2. Numerical treatments and optimization algorithm

We solve numerically the system of governing equations, discussed in the previous section, using the FDTD method [13]. We adopt the auxiliary differential equation approach to implement the Drude model in the FDTD method, and the uniaxial perfectly matched layer (UPML) is used to simulate the open-space radiation boundary condition [13,40]. The computational domain is discretized into uniform square (2D) or cubical (3D) Yee cells with spatial steps $\Delta x = \Delta y = \Delta z$ in all Cartesian directions.

In the forward system, we use the FDTD method and discretize the electric field at full-time indices and the magnetic field at half-time indices. In the adjoint system, however, the FDTD

discretization of the electric- and magnetic fields are performed at half-time indices and full-time indices, respectively [25,30]. The discretized objective function is

$$\tilde{W} = \frac{\varepsilon_0 \Delta t (\Delta x)^3}{2} \sum_{\Omega_d} \sum_{n=0}^N (\tilde{\mathcal{E}}^n)^2 \quad (24)$$

where $\tilde{\mathcal{E}}^n$ is the discretized electric field at time index n , Δt is the FDTD's temporal discretization step, and N is the number of time steps used in the simulations. Based on the FDTD discretization, the pointwise derivatives of the gradient expressions, given in Section 3.1, are

$$\frac{\partial \tilde{W}}{\partial \psi_i} = -\frac{\Delta t (\Delta x)^3}{\psi_i} \sum_{n=0}^N \tilde{\mathcal{E}}_i^{N-n} \frac{\tilde{\mathcal{J}}_i^{*n+\frac{1}{2}} + \tilde{\mathcal{J}}_i^{*n-\frac{1}{2}}}{2} \quad (25a)$$

$$\frac{\partial \tilde{W}}{\partial \varepsilon_{\infty i}} = -\varepsilon_0 (\Delta x)^3 \sum_{n=0}^N \tilde{\mathcal{E}}_i^{N-n} (\tilde{\mathcal{E}}_i^{*n+\frac{1}{2}} - \tilde{\mathcal{E}}_i^{*n-\frac{1}{2}}) \quad (25b)$$

$$\frac{\partial \tilde{W}}{\partial \sigma_i} = -\Delta t (\Delta x)^3 \sum_{n=0}^N \tilde{\mathcal{E}}_i^{N-n} \frac{\tilde{\mathcal{E}}_i^{*n+\frac{1}{2}} + \tilde{\mathcal{E}}_i^{*n-\frac{1}{2}}}{2} \quad (25c)$$

where i denotes the index of the i^{th} edge in Ω_d . Note that the temporal averaging of the discrete adjoint fields in Eqs. (25a) and (25c) is related to the time shift between the forward and the adjoint discrete systems [30].

To avoid mesh-dependency or self-penalization issues, in density-based TopOpt it is common to filter the design variables [48–52]. That is, instead of using ρ_i in Eq. (5), we replace it with $\tilde{\rho}_i$, where the filtered design vector $\tilde{\rho}$ is obtained through the mapping

$$\tilde{\rho} = \mathcal{F}(\rho). \quad (26)$$

In this work, we use an open-close, nonlinear filter operator $\mathcal{F}(\cdot)$ that consists of a cascade of four fW -mean filters [52]. The filter has two tuning parameters that determine its size and the level of nonlinearity. Here, we fix the filter size to a constant value of $5\Delta x$ and only employ the nonlinearity parameter to smoothly decrease the level of greyness in the design during the optimization process [52,53]. Using the chain rule, the derivative of the discrete objective function with respect to the design variable ρ_i is evaluated by

$$\frac{\partial \tilde{W}}{\partial \rho_i} = \frac{\partial \tilde{\rho}_i}{\partial \rho_i} \frac{\partial \psi_i}{\partial \tilde{\rho}_i} \frac{\partial \tilde{W}}{\partial \psi_i} + \frac{\partial \tilde{\rho}_i}{\partial \rho_i} \frac{\partial \varepsilon_{\infty i}}{\partial \tilde{\rho}_i} \frac{\partial \tilde{W}}{\partial \varepsilon_{\infty i}} + \frac{\partial \tilde{\rho}_i}{\partial \rho_i} \frac{\partial \sigma_i}{\partial \tilde{\rho}_i} \frac{\partial \tilde{W}}{\partial \sigma_i}. \quad (27)$$

We compared the derivatives computed using Eq. (27) against those evaluated by finite differences. The comparison showed more than 4 digits match in precision between the two methods. We write the discrete version of the optimization problem as

$$\begin{aligned} & \underset{\rho}{\text{maximize}} && \tilde{W} \\ & \text{subject to:} && \text{the governing equations,} \\ & && \text{a specified spectral content,} \\ & && 0 < \rho_i < 1, \end{aligned} \quad (28)$$

which we solve iteratively through the solution of a sequence of subproblems. Fig. 3 shows the flowchart of the optimization algorithm that we use to solve problem (28). To update the design variables, we use the globally convergent method of moving asymptotes (GCMMA) [54]. As a stopping criterion for the inner iteration loop, we monitor the norm of the first-order optimality condition after 12 iterations. Then, we mark the decrease of this norm by 70% as the termination condition of a subproblem. For the termination of the outer loop, we monitor the decrease of the level of non-discreteness, $\zeta = 4\tilde{\rho}^T(\mathbf{1} - \tilde{\rho})/M$ with $\mathbf{1}$ denoting a vector of a length M and all entries equal one [49]. We terminate the optimization process either when the value of ζ decreases below $\zeta_{\min} = 0.5\%$ or a maximum number of 600 iterations is reached. Then, the entries of the obtained design are thresholded around $\rho_{\text{th}} = 0.5$ to yield the final design.

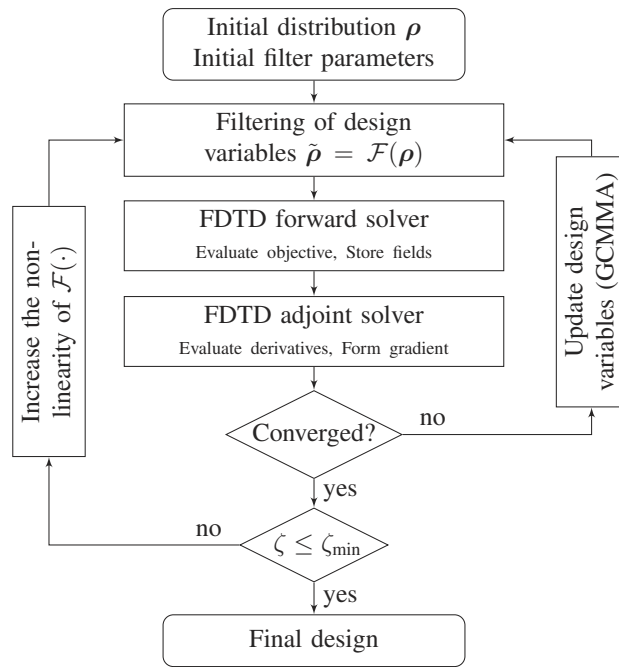


Fig. 3. Flowchart of the optimization algorithm.

4. Results

In this section, we demonstrate our method through some design examples of 2D and 3D plasmonic nanostructures. In 2D, only the case of TM excitation is presented. In fact, TE excitation does not lead to plasmonic effects, and the optimization algorithm shows regular convergence to traditional focusing mirror structures. To enable fast simulation, we implement the FDTD method to execute on graphics processing units (GPUs). The computations are executed on nodes equipped with NVidia V100 GPUs and 64 GB of memory. Based on the problem size, one call to the Maxwell solver uses a simulation time between less than a minute and few minutes.

4.1. 2D, TM nanoantennas

We chose a design domain Ω_d with dimensions $w_d = h_d = 100$ nm, and the observation domain Ω_g is centered within Ω_d and has dimensions $w_g = h_g = 10$ nm, see Fig. 1(a). We use a space-step $\Delta x = 0.5$ nm, and a time-step Δt satisfying the Courant stability criterion. The simulation domain is truncated by 15 UPML cells placed 30 cells away from Ω_d . The excitation is an \mathcal{H}_x polarized plane-wave propagating towards the positive y axis. The excitation spectrum has a bandwidth of 20% at half-maximum and is centered at 413 nm, as shown in Fig. 4(c) along with the results of optimization. The design variables are mapped to the in-plane permittivity components associated with the Yee edges where the electric field components \mathcal{E}_y and \mathcal{E}_z are located. Excluding the observation region, the design domain includes 79 560 design edges.

Figure 4(a) shows the progress of the normalized objective function \tilde{W} versus the iteration numbers. We start the algorithm with a uniform initial distribution $\rho_i = 0.5$ for all design variables. Included in the same figure are some snapshots to show the development of the design. The black color indicates silver ($\rho = 1$) and the white color indicates air ($\rho = 0$). Notably, the main topology of the antenna evolves after only a few tens of iterations. However, most of the late iterations are used to remove the intermediate material and form crisp boundaries, while the objective

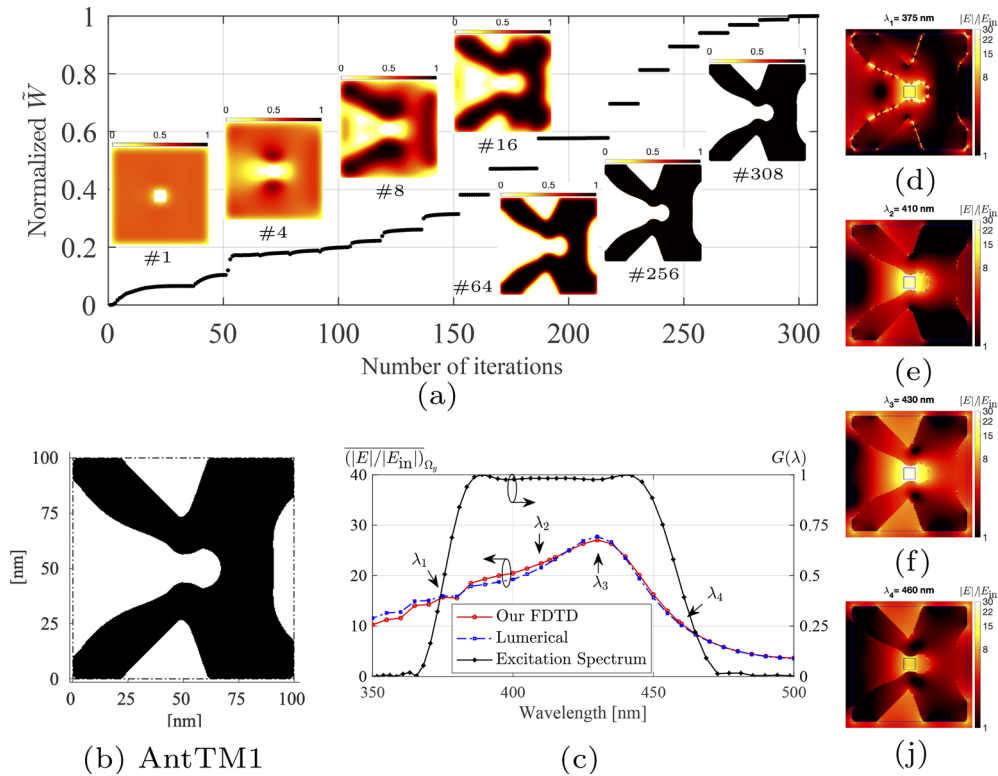


Fig. 4. (a) Progress of the objective function and some samples showing the development of AntTM1 (see Visualization 1). (b) AntTM1 topology. (c) Average field enhancement in Ω_g together with the excitation spectrum. (d)-(j) Field distribution at $\lambda = 375, 410, 430,$ and 460 nm.

function keeps increasing monotonically. The design algorithm converged after 308 iterations to a design with a grayness level $\zeta < 0.2\%$. We threshold this design around $\rho_{th} = 0.5$ and show the final design, AntTM1, in Fig. 4(b). On the side facing the incident wave, the topology of AntTM1 developed as a flared horn, backed by a small cavity region. On the other side, we see two slightly tilted vertical arms. This optimized topology shares similarities with results reported in the literature using the FEM method [37].

Fig. 4(c) shows the average field enhancement of AntTM1 at Ω_g , which correlates well with the excitation spectrum shown in the same figure. We cross-validate our computations with the commercial software package Ansys Lumerical FDTD [55]. Slight differences between the two computations are attributed to differences in geometry descriptions. Inside Ω_g and within the excitation window, AntTM1 exhibits more than 20-fold field enhancement. The peak of the performance, $(|E|/|E_{in}|)_{\Omega_g} = 27.8$, occurs at the wavelength $\lambda = 430$ nm, which resides at long wavelengths in the excitation window. Figs. 4(d)-(j) show the electric field distribution of AntTM1 at four wavelengths, marked in Fig. 4(c). The electric field is maximum at Ω_g , marked by the box at the center. However, we observe a field localization and enhancement at the device's boundaries for short wavelengths, which justifies the decrease of the energy enhancement in Ω_g at short wavelengths. We attempt to improve the optimization results further by exploring the following investigations.

4.1.1. Effect of the design domain size

The design obtained in Fig. 4 hits the boundary of the design domain, which suggests the need for a larger design space. We double the size of the design domain to $200 \times 200 \text{ nm}^2$, and we solve the optimization problem, which now includes 319 960 design variables. The algorithm converged in 297 iterations to the topology shown in Fig. 5(a). The new design, AntTM2, has more topological features compared to AntTM1. We observe an additional vertical arm that evolved in the rear-side of the device, and the arm around Ω_g appears straight. The performance of AntTM2 has improved at short wavelengths, and it attains a nearly flat response within the excitation window, as shown in Fig. 5(b). Fig. 5(c) shows the field distribution at $\lambda = 440 \text{ nm}$.

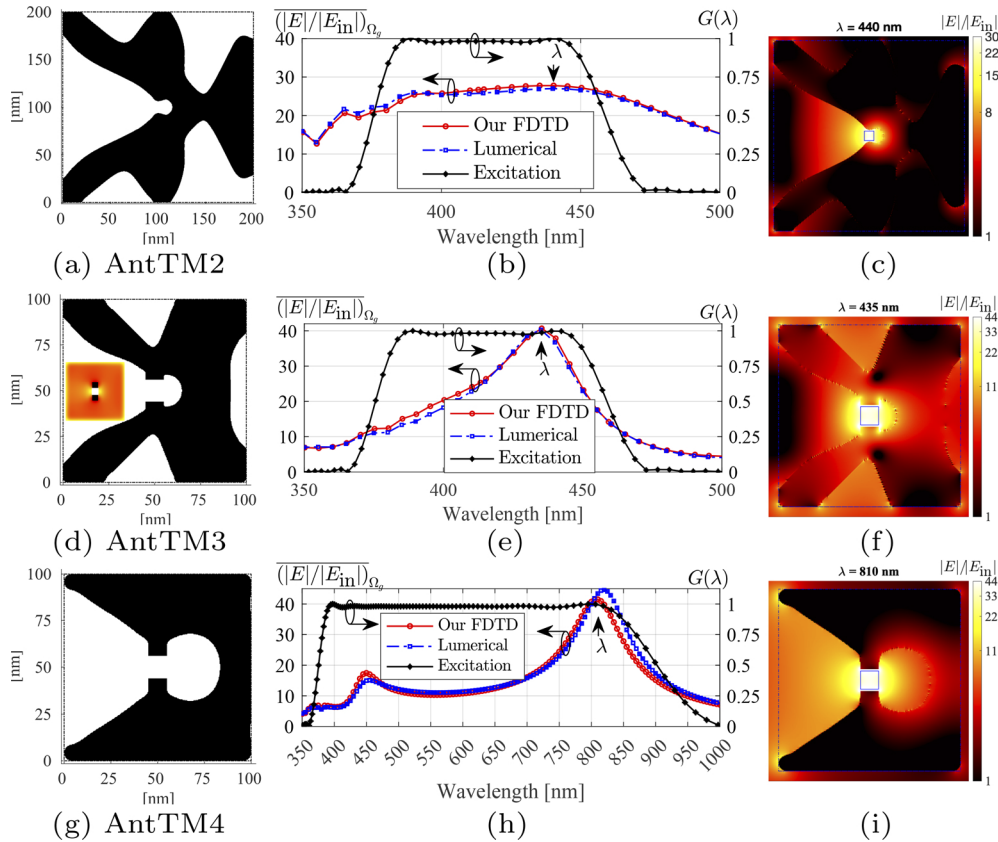


Fig. 5. Topology, average field enhancement in Ω_g , and field distribution at wavelength of maximum performance for (a)-(c) AntTM2 (see Visualization 2), (d)-(f) AntTM3 (see Visualization 3), and (g)-(i) AntTM4 (see Visualization 4), respectively. The colored insets in (d) shows the design at iteration #1.

4.1.2. Effect of a fixed gap geometry

Maximizing the energy in Ω_g suggests that the objective function is more sensitive to design variables close to Ω_g compared to those away from it. We attempt to relax such a non-uniform sensitivity distribution and investigate its effect on the results. We fix the geometry region below and above Ω_g to silver with the same area as Ω_g . Figs. 5(d)-(f) shows AntTM3 optimized over a design domain with size $100 \times 100 \text{ nm}^2$. For AntTM3, fixing the area around the gap boosts the average field enhancement to a maximum value of 40.6 at the wavelength 435 nm; AntTM1 has a

maximum value of 27.8. The new nanoantenna exhibits better performance at long wavelengths, however, the performance at short wavelengths stays essentially the same as in the previous cases. These results indicate the challenges that plasmonic effects pose on optimizing nanoantennas near the surface plasmon frequency.

4.1.3. Wideband optimization

We use the previous setup and attempt to optimize over a wider spectrum covering the wavelength window 375–900 nm. That is, we use an excitation signal with a half-maximum bandwidth of 82% centered around 637.5 nm. Figs. 5(g)-(i) show the topology, the average field enhancement, and the field distribution at the wavelength of maximum performance for the new design. The new nanoantenna, AntTM4, shows a wideband performance. An average field enhancement above 10-fold is possible to achieve. Moreover, the average field enhancement hits a maximum of 41.5 at the wavelength 810 nm. Here, we still observe the performance bias of the optimized nanoantennas towards long wavelengths.

4.2. 3D antennas

We use the developed method to optimize antennas in a 3D setup. We extend the problem model (Fig. 1) to include a 30 nm thickness in the x -direction. The design space has a volume $\Omega_d = 200 \times 200 \times 30 \text{ nm}^3$ with $\Omega_g = 12 \times 12 \times 30 \text{ nm}^3$, and we use $\Delta x = 2 \text{ nm}$. Similar to the 2D case, here we fix the geometry region below and above Ω_g to silver with the same area as Ω_g . The discretized design domain includes 469 341 design variables associated with its interior edges. We impose symmetry along the x -axis to enable antennas producible by current technologies. That is, we optimize 3D antennas and aim for planar structures. The excitation is an \mathcal{E}_z polarized plane-wave propagating in the positive x axis. We use the same setup and solve the optimization problem for three different wavelength excitation windows. The first and second excitation spectra, shown in Fig. 6(a), have a half-maximum bandwidth of 20% centered around 413 nm and 513 nm, respectively. The third excitation spectrum, shown in Fig. 6(b), has a half-maximum bandwidth covering the spectral window 375–900 nm. Each excitation spectrum results in a different topology which we name Ant3D1, Ant3D2, and Ant3D3, see Figs. 6(c)-(e). Interestingly, we observe the increase of the figure-of-eight void area of the three nanoantennas, around Ω_g , as the excitation spectrum includes long wavelengths.

Fig. 6(a) shows the average field enhancement of Ant3D1 and Ant3D2, and Fig. 6(b) shows the performance of Ant3D3. Inside Ω_g , the nanoantennas Ant3D1, Ant3D2, and Ant3D3 exhibit a maximum average field enhancement of 50.5, 52.8, and 46.7 at the wavelength 445 nm, 545 nm, and 615 nm, respectively. Ant3D3 exhibits another peak of 74.0 at 970 nm, which resides slightly outside the intended excitation spectrum. The optimized structures tend to exhibit a better field enhancement at long wavelengths. Figs. 6(f)-(i) show the field distribution of Ant3D3 at wavelengths marked in Figs. 6(b). The optimized structures are capable to maximize the electric energy at the observation domain Ω_g . At short wavelengths, however, we observe high-field localization near nanoantenna's boundaries, which indicates strong plasmonic effects that are responsible for the decrease in the achieved performance. Further investigations are needed to obtain a balanced performance over the wavelength window of interest.

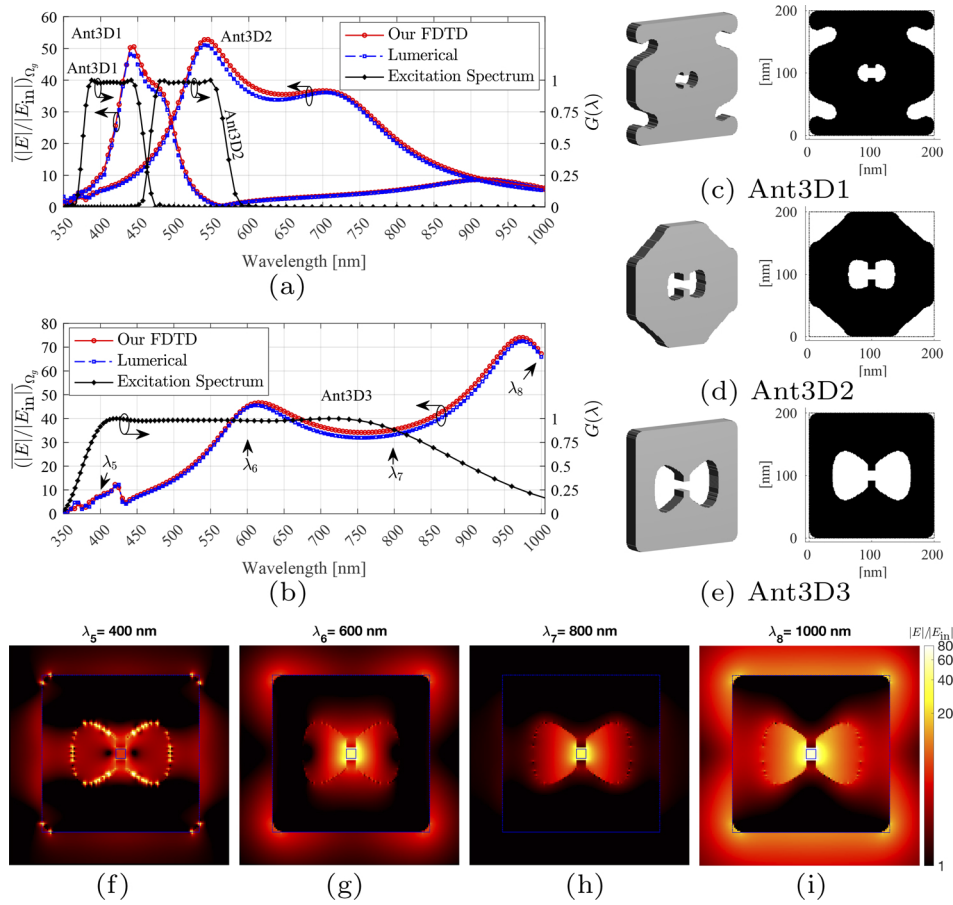


Fig. 6. Average field enhancements inside Ω_g together with the excitation spectrum for (a) Ant3D1 and Ant3D2, (b) Ant3D3. Topologies of (c) Ant3D1 (see Visualization 5), (d) Ant3D2 (see Visualization 6), and (e) Ant3D3 (see Visualization 7). Field enhancements at the middle layer of (f)-(i) Ant3D1 at wavelengths marked in Fig. 6(b).

5. Conclusion

We introduced a density-based TopOpt approach to design plasmonic dispersive nanoantennas. Our approach is based on Maxwell's equations in the time-domain, and we use the Drude model, which can fit the material dispersion of metals and conductive polymers, as well as epsilon-near-zero materials, such as conductive oxides. For the TM and the 3D setups, the interpolation between metallic and dielectric phases results in high field-localization associated with plasmonic effects, which prevent the algorithm from converging to well-performing designs. Guided by dispersion diagrams of metal-dielectric interfaces, we proposed an artificial damping approach to suppress the field-localization during the optimization process, which enables the algorithm to converge to good designs. For the TE setup, artificial damping is not needed and the algorithm encounters no convergence issues. Various setups for narrowband and wideband optimization are presented, resulting in novel 2D and 3D nanoantenna designs with outstanding performances. Our method opens new opportunities for the automatic design and optimization of dispersive nanophotonic structures with broadband optical response for applications in nonlinear plasmonics, integrated optics, plasmonic colouring and absorbers, epsilon-near-zero photonics, thermoplasmonics, biosensors, and ultrafast optics.

Funding. Deutsche Forschungsgemeinschaft (EXC 2122, Project ID 390833453); Bundesministerium für Bildung und Forschung.

Acknowledgement. The computations were performed on resources provided by the Swedish National Infrastructure for Computing (SNIC) at HPC2N center; the central computing cluster operated by Leibniz University IT Services (LUIS); and the North German Supercomputing Alliance (HLRN). A.C.L. acknowledges the German Federal Ministry of Education and Research (BMBF) under the Tenure-Track Program. The publication of this article was funded by the Open Access Fund of the Leibniz Universität Hannover. We acknowledge the Deutsche Forschungsgemeinschaft (DFG, German Research Foundation) under Germany's Excellence Strategy within the Cluster of Excellence PhoenixD (EXC 2122, Project ID 390833453).

Disclosures. The authors declare no conflicts of interest.

Data availability. Data underlying the results presented in this paper are not publicly available at this time but may be obtained from the authors upon reasonable request.

References

1. N. Yu, P. Genevet, M. A. Kats, F. Aieta, J.-P. Tetienne, F. Capasso, and Z. Gaburro, "Light Propagation with Phase Discontinuities: Generalized Laws of Reflection and Refraction," *Science* **334**(6054), 333–337 (2011).
2. S. M. Kamali, E. Arbabi, A. Arbabi, and A. Faraon, "A review of dielectric optical metasurfaces for wavefront control," *Nanophotonics* **7**(6), 1041–1068 (2018).
3. E. Karimi, S. A. Schulz, I. De Leon, H. Qassim, J. Upham, and R. W. Boyd, "Generating optical orbital angular momentum at visible wavelengths using a plasmonic metasurface," *Light: Sci. Appl.* **3**(5), e167 (2014).
4. J.-M. Guay, A. Calà Lesina, G. Côté, M. Charron, D. Poitras, L. Ramunno, P. Berini, and A. Weck, "Laser-induced plasmonic colours on metals," *Nat. Commun.* **8**(1), 16095 (2017).
5. M. L. Tseng, Y. Jahani, A. Leitis, and H. Altug, "Dielectric Metasurfaces Enabling Advanced Optical Biosensors," *ACS Photonics* **8**(1), 47–60 (2021).
6. G. Baffou, F. Cichos, and R. Quidant, "Applications and challenges of thermoplasmonics," *Nat. Mater.* **19**(9), 946–958 (2020).
7. A. Calà Lesina, D. Goodwill, E. Bernier, L. Ramunno, and P. Berini, "Tunable plasmonic metasurfaces for optical phased arrays," *IEEE J. Sel. Top. Quantum Electron.* **27**(1), 1–16 (2021).
8. J. Lee, M. Tymchenko, C. Argyropoulos, P.-Y. Chen, F. Lu, F. Demmerle, G. Boehm, M.-C. Amann, A. Alù, and M. A. Belkin, "Giant nonlinear response from plasmonic metasurfaces coupled to intersubband transitions," *Nature* **511**(7507), 65–69 (2014).
9. A. Calà Lesina, P. Berini, and L. Ramunno, "Vectorial control of nonlinear emission via chiral butterfly nanoantennas: generation of pure high order nonlinear vortex beams," *Opt. Express* **25**(3), 2569–2582 (2017).
10. S. Rashid, J. Walia, H. Northfield, C. Hahn, A. Olivieri, A. C. Lesina, F. Variola, A. Weck, L. Ramunno, and P. Berini, "Helium ion beam lithography and liftoff," *Nano Futures* **5**(2), 025003 (2021).
11. S. Molesky, Z. Lin, A. Y. Piggott, W. Jin, J. Vucković, and A. W. Rodriguez, "Inverse design in nanophotonics," *Nat. Photonics* **12**(11), 659–670 (2018).
12. S. D. Campbell, D. Sell, R. P. Jenkins, E. B. Whiting, J. A. Fan, and D. H. Werner, "Review of numerical optimization techniques for meta-device design," *Opt. Mater. Express* **9**(4), 1842–1863 (2019).
13. A. Taflov and S. Hagness, *Computational Electrodynamics: The Finite-Difference Time-Domain Method* (Artech House, 2005), 3rd ed.
14. J.-M. Jin, *The finite element method in electromagnetics* (Wiley, 2014), 3rd ed.
15. O. Sigmund, "On the usefulness of non-gradient approaches in topology optimization," *Struct. Multidiscip. Optim.* **43**(5), 589–596 (2011).
16. J. Baxter, A. Calà Lesina, J.-M. Guay, A. Weck, P. Berini, and L. Ramunno, "Plasmonic colours predicted by deep learning," *Sci. Rep.* **9**(1), 8074 (2019).
17. Y. Chen, L. Lu, G. E. Karniadakis, and L. D. Negro, "Physics-informed neural networks for inverse problems in nano-optics and metamaterials," *Opt. Express* **28**(8), 11618–11633 (2020).
18. W. Ma, Z. Liu, Z. A. Kudyshev, A. Boltasseva, W. Cai, and Y. Liu, "Deep learning for the design of photonic structures," *Nat. Photonics* **15**(2), 77–90 (2021).
19. M. P. Bendsøe and O. Sigmund, *Topology Optimization* (Springer Berlin Heidelberg, 2004).
20. J. D. Deaton and R. V. Grandhi, "A survey of structural and multidisciplinary continuum topology optimization: post 2000," *Struct. Multidiscip. Optim.* **49**(1), 1–38 (2014).
21. M. P. Bendsøe and N. Kikuchi, "Generating optimal topologies in structural design using a homogenization method," *Comput. Methods Appl. Mech. Eng.* **71**(2), 197–224 (1988).
22. E. Wadbro and M. Berggren, "Topology optimization of an acoustic horn," *Comput. Methods Appl. Mech. Eng.* **196**(1-3), 420–436 (2006).
23. A. Gersborg-Hansen, O. Sigmund, and R. Haber, "Topology optimization of channel flow problems," *Struct. Multidiscip. Optim.* **30**(3), 181–192 (2005).
24. T. Nomura, K. Sato, K. Taguchi, T. Kashiwa, and S. Nishiwaki, "Structural topology optimization for the design of broadband dielectric resonator antennas using the finite difference time domain technique," *Int. J. Num. Meth. Eng.* **71**(11), 1261–1296 (2007).

25. E. Hassan, E. Wadbro, and M. Berggren, "Topology optimization of metallic antennas," *IEEE Trans. Antennas Propag.* **62**(5), 2488–2500 (2014).
26. N. Aage and V. Egede Johansen, "Topology optimization of microwave waveguide filters," *Int. J. Numer. Meth. Eng.* **112**(3), 283–300 (2017).
27. J. Wang, X.-S. Yang, X. Ding, and B.-Z. Wang, "Antenna radiation characteristics optimization by a hybrid topological method," *IEEE Trans. Antennas Propag.* **65**(6), 2843–2854 (2017).
28. E. Hassan, B. Scheiner, F. Michler, M. Berggren, E. Wadbro, F. Röhr, S. Zorn, R. Weigel, and F. Lurz, "Multilayer topology optimization of wideband SIW-to-waveguide transitions," *IEEE Trans. Microwave Theory Tech.* **68**(4), 1326–1339 (2020).
29. Y. Zhang, O. S. Ahmed, and M. H. Bakr, "Wideband FDTD-Based Adjoint Sensitivity Analysis of Dispersive Electromagnetic Structures," *IEEE Trans. Microw. Theory Tech.* **62**(5), 1122–1134 (2014).
30. E. Hassan, E. Wadbro, and M. Berggren, "Time-domain sensitivity analysis for conductivity distribution in Maxwell's equations," Tech. Rep. UMINF 15.06, Dept. of Computing Science, Umeå University (2015).
31. N. Aage, E. Andreassen, B. S. Lazarov, and O. Sigmund, "Giga-voxel computational morphogenesis for structural design," *Nature* **550**(7674), 84–86 (2017).
32. J. Jensen and O. Sigmund, "Topology optimization for nano-photonics," *Laser Photonics Rev.* **5**(2), 308–321 (2010).
33. Y. Elesin, B. Lazarov, J. Jensen, and O. Sigmund, "Time domain topology optimization of 3D nanophotonic devices," *Photonics Nanostructures: Fundam. Appl.* **12**(1), 23–33 (2014).
34. L. F. Frellsen, Y. Ding, O. Sigmund, and L. H. Frandsen, "Topology optimized mode multiplexing in silicon-on-insulator photonic wire waveguides," *Opt. Express* **24**(15), 16866–16873 (2016).
35. Y. Augenstein and C. Rockstuhl, "Inverse design of nanophotonic devices with structural integrity," *ACS Photonics* **7**(8), 2190–2196 (2020).
36. E. Wadbro and C. Engström, "Topology and shape optimization of plasmonic nano-antennas," *Comput. Methods Appl. Mech. Eng.* **293**, 155–169 (2015).
37. R. E. Christiansen, J. Vester-Petersen, S. P. Madsen, and O. Sigmund, "A non-linear material interpolation for design of metallic nano-particles using topology optimization," *Comput. Methods Appl. Mech. Eng.* **343**, 23–39 (2019).
38. Z. Zeng, P. K. Venuthurumilli, and X. Xu, "Inverse design of plasmonic structures with FDTD," *ACS Photonics* **8**(5), 1489–1496 (2021).
39. V. Giannini, A. I. Fernández-Domínguez, S. C. Heck, and S. A. Maier, "Plasmonic Nanoantennas: Fundamentals and their use in controlling the radiative properties of nanoemitters," *Chem. Rev.* **111**(6), 3888–3912 (2011).
40. M. Okoniewaki, M. Mrozowski, and M. Stuchly, "Simple treatment of multi-term dispersion in FDTD," *IEEE Microw. Guid. Wave Lett.* **7**(5), 121–123 (1997).
41. K. P. Prokopidis and D. C. Zografopoulos, "A Unified FDTD/PML Scheme Based on Critical Points for Accurate Studies of Plasmonic Structures," *J. Lightwave Technol.* **31**(15), 2467–2476 (2013).
42. A. Vial, A.-S. Grimault, D. Macías, D. Barchiesi, and M. L. de la Chapelle, "Improved analytical fit of gold dispersion: Application to the modeling of extinction spectra with a finite-difference time-domain method," *Phys. Rev. B* **71**(8), 085416 (2005).
43. M. Z. Alam, I. D. Leon, and R. W. Boyd, "Large optical nonlinearity of indium tin oxide in its epsilon-near-zero region," *Science* **352**(6287), 795–797 (2016).
44. J. Karst, M. Floess, M. Ubl, C. Dingler, C. Malacrida, T. Steinle, S. Ludwigs, M. Hentschel, and H. Giessen, "Electrically switchable metallic polymer nanoantennas," *Science* **374**(6567), 612–616 (2021).
45. H. Raether, *Surface plasmons: on smooth and rough surfaces and on gratings*, 111 (Springer, Berlin, 1988).
46. S. A. Maier, *Plasmonics: Fundamentals and Applications* (Springer US, New York, NY, 2007).
47. K. M. McPeak, S. V. Jayanti, S. J. P. Kress, S. Meyer, S. Iotti, A. Rossinelli, and D. J. Norris, "Plasmonic films can easily be better: Rules and recipes," *ACS Photonics* **2**(3), 326–333 (2015).
48. T. Borrvall, "Topology optimization of elastic continua using restriction," *Arch. Comput. Methods Engrg.* **8**(4), 351–385 (2001).
49. O. Sigmund, "Morphology-based black and white filters for topology optimization," *Struct. Multidiscip. Optim.* **33**(4-5), 401–424 (2007).
50. K. Svanberg and H. Svärd, "Density filters for topology optimization based on the pythagorean means," *Struct. Multidiscip. Optim.* **48**(5), 859–875 (2013).
51. E. Hassan, E. Wadbro, and M. Berggren, "Patch and ground plane design of microstrip antennas by material distribution topology optimization," *Prog. Electromagn. Res. B* **59**, 89–102 (2014).
52. L. Hägg and E. Wadbro, "Nonlinear filters in topology optimization: existence of solutions and efficient implementation for minimum compliance problems," *Struct. Multidiscip. Optim.* **55**(3), 1017–1028 (2017).
53. E. Hassan, E. Wadbro, L. Hägg, and M. Berggren, "Topology optimization of compact wideband coaxial-to-waveguide transitions with minimum-size control," *Struct. Multidiscip. Optim.* **57**(4), 1765–1777 (2018).
54. K. Svanberg, "A class of globally convergent optimization methods based on conservative convex separable approximations," *SIAM J. Optim.* **12**(2), 555–573 (2002).
55. Ansys, Lumerical version 2020-2.4," <https://www.ansys.com/products/photonics/fdtd>. Last accessed Dec. 2021.